Astronomy & Astrophysics

VLA cm-wave survey of young stellar objects in the Oph A cluster: constraining extreme UV- and X-ray-driven disk photoevaporation

A pathfinder for Square Kilometre Array studies[*]

A. Coutens[1], H. B. Liu[2], I. Jiménez-Serra[3], T. L. Bourke[4], J. Forbrich[5], M. Hoare[6], L. Loinard[7,8], L. Testi[2,9], M. Audard[10,11], P. Caselli[12], A. Chacón-Tanarro[13], C. Codella[9,14], J. Di Francesco[15,16], F. Fontani[9], M. Hogerheijde[17,18], A. Johansen[19], D. Johnstone[15,16], S. Maddison[20], O. Panić[6], L. M. Pérez[21], L. Podio[9], A. Punanova[22], J. M. C. Rawlings[23], D. Semenov[24,25], M. Tazzari[26], J. J. Tobin[27], M. H. D. van der Wiel[28], H. J. van Langevelde[29,16], W. Vlemmings[30], C. Walsh[6], and D. Wilner[31]

(Affiliations can be found after the references)

ABSTRACT

Observations of young stellar objects (YSOs) in centimeter bands can probe the continuum emission from growing dust grains, ionized winds, and magnetospheric activity that are intimately connected to the evolution of protoplanetary disks and the formation of planets. We carried out sensitive continuum observations toward the Ophiuchus A star-forming region, using the *Karl G. Jansky* Very Large Array (VLA) at 10 GHz over a field-of-view of 6′ and with a spatial resolution of $\theta_{maj} \times \theta_{min} \sim 0.\!''4 \times 0.\!''2$. We achieved a 5 μJy beam^{-1} rms noise level at the center of our mosaic field of view. Among the 18 sources we detected, 16 were YSOs (three Class 0, five Class I, six Class II, and two Class III) and two were extragalactic candidates. We find that thermal dust emission generally contributed less than 30% of the emission at 10 GHz. The radio emission is dominated by other types of emission, such as gyro-synchrotron radiation from active magnetospheres, free–free emission from thermal jets, free–free emission from the outflowing photoevaporated disk material, and synchrotron emission from accelerated cosmic-rays in jet or protostellar surface shocks. These different types of emission could not be clearly disentangled. Our non-detections for Class II/III disks suggest that extreme UV-driven photoevaporation is insufficient to explain disk dispersal, assuming that the contribution of UV photoevaporating stellar winds to radio flux does not evolve over time. The sensitivity of our data cannot exclude photoevaporation due to the role of X-ray photons as an efficient mechanism for disk dispersal. Deeper surveys using the Square Kilometre Array (SKA) will have the capacity to provide significant constraints to disk photoevaporation.

Key words. stars: formation – protoplanetary disks – radio continuum: stars – stars: activity

1. Introduction

The first step towards forming the building blocks of planets occurs via grain growth in disks composed of dust and gas surrounding young stars (e.g., Testi et al. 2014; Johansen et al. 2014). Thus, the time available for the formation of planets is limited by the lifetime of the disk. After 10 Myr, the majority of disks disappear (e.g., Haisch et al. 2005; Russell et al. 2006; Williams & Cieza 2011; Ribas et al. 2015). Understanding the mechanisms that lead to disk dispersal and the time-scales involved is crucial in characterizing the environment in which planets are formed.

The detection of transition disks where dust has been cleared within the inner regions (e.g., Strom et al. 1989; Pascucci et al. 2016; van der Marel et al. 2018; Ansdell et al. 2018) has favored the development of theoretical models where disk dispersal occurs from the inside out (e.g., photoevaporation, grain growth, giant planet formation). In particular, models of disk dispersal through photoevaporation can successfully explain inner hole sizes and accretion rates for a large number of transition disks

(e.g., Alexander & Armitage 2009; Owen et al. 2011, 2012; Ercolano et al. 2018). Given that radio observations trace ionized material, they could therefore provide useful constraints on different photoevaporation models (Pascucci et al. 2012; Macías et al. 2016). Moreover, radio observations are also useful for tracing the magnetospheric activity of young stellar objects (YSOs), as well as grain growth process in disks (Güdel 2002; Forbrich et al. 2007, 2017; Choi et al. 2009; Guilloteau et al. 2011; Pérez et al. 2012; Liu et al. 2014; Tazzari et al. 2016).

The Ophiuchus A (Oph A) cluster is one of the nearest star-forming regions ($d \sim 137$ pc, Ortiz-León et al. 2017). Its proximity and the abundance of YSOs at a wide range of evolutionary stages (Gutermuth et al. 2009) make this cluster an ideal laboratory for studying the evolution of YSO radio activity. We present here the first results of new radio continuum observations of the Oph A region using the NRAO *Karl G. Jansky* Very Large Array (VLA) at 10 GHz, which have achieved an unprecedented level of sensitivity (5 μJy beam^{-1} in the center of the field). In Sect. 2, we describe the observations and data reduction. In Sect. 3, we present the sources that have been detected and we analyze the nature of the continuum emission detected towards the YSOs. In Sect. 4, we discuss the contribution of the extreme ultraviolet (EUV) and X-ray photoevaporation in the dispersal of
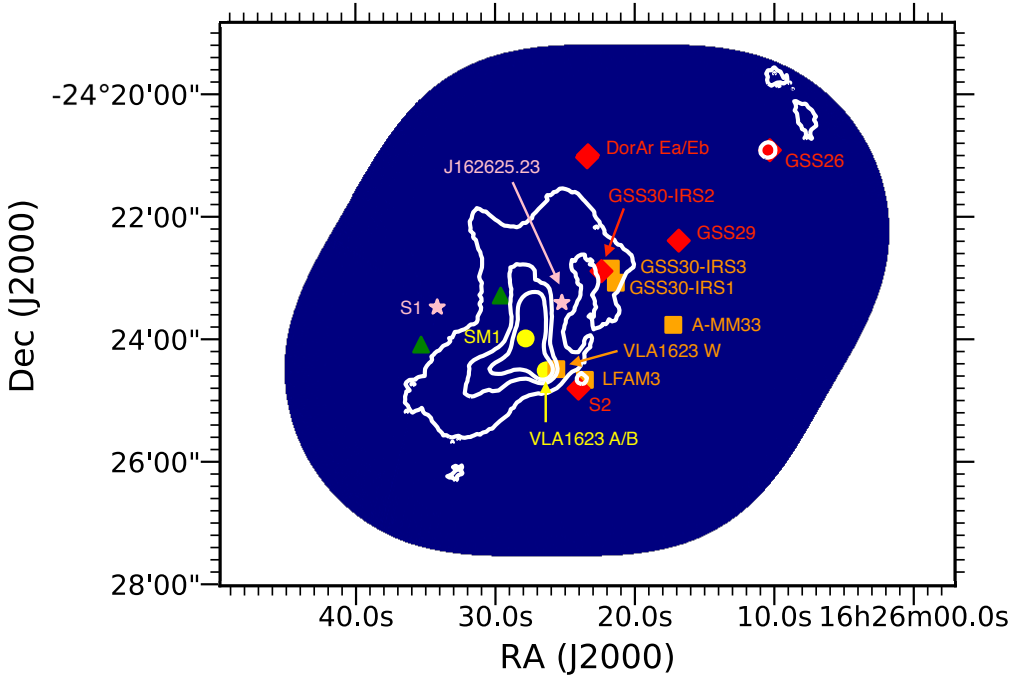

Fig. 1. Field of view covered by VLA X band observations shown in blue. The position of the detected Class 0, I, II and III sources are indicated with yellow circles, orange squares, red diamonds, and pink stars, respectively. Sources VLA1623 and DoAr 24E are binary systems. The extragalactic candidates are indicated with green triangles. White contours represent 850 μm continuum observations from the JCMT Gould Belt Survey taken by SCUBA-2 (Pattle et al. 2015; Kirk et al. 2018).

disks in Oph A, and the prospects related to the upcoming Square Kilometre Array (SKA).

2. Observations

We performed five epochs of mosaic observations towards the Oph A YSO cluster at X band (8.0–12.0 GHz) using the VLA (project code: 16B-259, PI: Audrey Coutens). All five epochs of observation (see Table 1) were carried out in the most extended, A array configuration, which provides a projected baseline range from 310 to 34 300 m. We used the 3-bit samplers and configured the correlator to have 4 GHz of continuous bandwidth coverage centered on the sky frequency of 10 GHz divided into 32 contiguous spectral windows. The pointing centers of our observations are given in Table 2. They are separated by 2.6′, while the primary beam FWHM is 4.2′. In each epoch of observation, the total on-source observing time for each pointing was 312 s. The quasar J1625-2527 was observed approximately every 275 s for complex gain calibration. We observed 3C286 as the absolute flux reference. The joint imaging of these mosaic fields forms an approximately parallelogram-shaped, mosaic field of view, of which the width and height are ~6′. Figure 1 shows the observed field of view.

We calibrated the data manually using the CASA[1] software package, following standard data calibration procedures. To maximize sensitivity, we combined the data from all five epochs of observation. We ensured that highly variable sources did not affect the image quality or the results by additionally imaging the individual epochs separately (see Sect. 3.2.2). The imaging was done with Briggs robust = 2.0 weighting, gridder = "mosaic", specmode = "mfs", and nterms = 1. This setting was used to maximize signal-to-noise ratio (S/N) ratios. Using >1 nterms is not suitable for this project given the sources are relatively faint. At the average observing frequency, we obtained a synthesized beam of $\theta_{\mathrm{maj}} \times \theta_{\mathrm{min}} \sim 0.\!''4 \times 0.\!''2$ and a maximum detectable angular scale of ~5″ (or ~700 au). After primary

---

[1] The Common Astronomy Software Applications software package, release 4.7.2 (McMullin et al. 2007).

Table 1. VLA observations.

Epoch	Starting time (UTC)	Initial API rms (°)	Projected baseline (m)	$F_{9.9\,\mathrm{GHz}}^{\mathrm{gain}}$ (Jy)
1	2016-12-02 21:31	11	310–34 300	1.4
2	2016-12-05 21:18	6.0	460–34 300	1.3
3	2017-01-06 18:05	13	325–32 800	1.4
4	2017-01-14 18:40	13	310–34 300	1.3
5	2017-01-22 17:12	4.4	665–33 100	1.3

Notes. API refers to Atmospheric Phase Interferometer, which observes an 11.7 GHz beacon from a geostationary satellite with a 300 meters baseline. $F_{9.9\,\mathrm{GHz}}^{\mathrm{gain}}$ is the measured flux of the gain calibrator J1625-2527.

Table 2. Mosaic pointings.

Name	RA (J2000)	Dec (J2000)
X1	$16^{\mathrm{h}}26^{\mathrm{m}}32^{\mathrm{s}}.00$	$-24°24'30.\!''0$
X2	$16^{\mathrm{h}}26^{\mathrm{m}}20^{\mathrm{s}}.62$	$-24°24'30.\!''0$
X3	$16^{\mathrm{h}}26^{\mathrm{m}}26^{\mathrm{s}}.31$	$-24°22'15.\!''0$
X4	$16^{\mathrm{h}}26^{\mathrm{m}}14^{\mathrm{s}}.93$	$-24°22'15.\!''0$

beam correction, we achieved a rms noise level of ~5 μJy beam^{-1} at the center of our mosaic field, degraded to ~28 μJy beam^{-1} toward the edges of the mosaic. The flux calibration uncertainty is expected to be about 5%.

3. Results

3.1. Source census and comparison with other surveys

In total, we detected 18 sources above 5σ in our mosaic field of view. The fluxes of the detected sources were measured by performing two-dimensional Gaussian fits, using the

`imfit` task of CASA. The derived fluxes and coordinates can be found in Table B.1, where the names of the sources Jhhmmss.ss-ddmmss.s are based on the coordinates of peak intensity obtained with the fitting procedure. The position uncertainties are typically about a few tens of mas. Table B.1 also lists the more commonly used names of these sources. When the source structure was too complex to be fitted with this method or the results of the fit were too uncertain, we measured the flux by integrating over a circular area around the source with CASA. Table A.1 summarizes the sizes measured with the Gaussian fit after deconvolution from the beam.

We compared our detections with the list of YSOs present in our field based on the photometric and spectroscopic surveys presented in Wilking et al. (2008), Jørgensen et al. (2008), Hsieh & Lai (2013), and Dzib et al. (2013). Dzib et al. (2013) carried out large-scale observations of the Ophiuchus region with the VLA at 4.5 and 7.5 GHz with a resolution of 1″. Wilking et al. (2008) used X-ray and infrared photometric surveys as well as spectroscopic surveys of the L1688 cloud to list all the association members present in the Two Micron All-Sky Survey (2MASS) catalog. They also classify sources according to their respective spectral energy distributions (SEDs) built from the *Spitzer* Cores to Disks (c2d) survey. Hsieh & Lai (2013) compile another list based on the c2d Legacy Project after developing a new method to identify fainter YSOs based on analyzing multi-dimensional magnitude space. Finally, Jørgensen et al. (2008) identify the more deeply embedded YSOs by jointly analyzing *Spitzer* and JCMT/SCUBA data. Overall, 18 of our detected sources have all been found in at least one previous catalog or study. Specifically, 16 of our 18 radio detections are associated with YSOs, while the remaining two are probably extragalactic sources (Dzib et al. 2013). Individual images of our detected YSOs are provided in Fig. 2. Sidelobes are visible for some of these sources (S1, SM1). In total, we detected 11 YSO candidates listed in the catalog of Wilking et al. (2008), while the remaining 19 YSOs in that catalog were undetected (see label "b" in Table B.1). Also, we detected nine of the sources listed by Hsieh & Lai (2013, see label "c" in Table B.1). Finally, we detected five of the young sources listed in Jørgensen et al. (2008), while two others (162614.63-242 507.5 and 162 625.49-242 301.6) were undetected.

Compared to the previous VLA survey at 4.5 and 7.5 GHz by Dzib et al. (2013, see Table B.1), we detected seven additional radio sources, namely J162627.83-242 359.4 (SM1, #3 in Table B.1), J162617.23-242 345.7 (A-MM33, #4), J162621.36-242 304.7 (GSS30-IRS1, #5), J162623.36-242 059.9 (DoAr 24Ea, #19), J162623.42-242 102.0 (DoAr 24Eb, #20), J162624.04-242 448.5 (S2, #21), and J162625.23-242 324.3 (#30). All of these are young stellar objects. Three sources reported in Dzib et al. (2013) were undetected in our observations. These three sources are extragalactic (EG) candidates. A possible explanation for these non-detections is that they have a negative spectral index. Hence, the observations at 4.5 and 7.5 GHz by Dzib et al. (2013) could be more sensitive to this type of target because of their greater brightness at a lower frequency. Another explanation would be that these sources are variable. We comment briefly on some of the individual young stellar objects below.

J162627.83-242 359.3 (also known as SM1, #3) was previously classified as a prestellar core (see Motte et al. 1998). It was, however, detected at 5 GHz with the VLA at an angular resolution of ∼10″ (measured peak fluxes of 130–200 μJy beam^{-1}; Leous et al. 1991; Gagné et al. 2004), although, in the first study, the source appears slightly offset by 3″. More recent ALMA observations suggest that SM1 is actually protostellar and that it hosts a warm (∼30–50 K) accretion disk or pseudo-disk (Friesen et al. 2014, 2018; Kirk et al. 2017).

The source J162623.42-242 101.9 (known as DoAr 24Eb, #20) is the companion of the protostar J162623.36-242 059.9 (DoAr 24Ea, #19), also detected in our dataset (see Fig. 2). These two sources are assumed to be at a similar evolutionary stage, although more data are needed to confirm this hypothesis (Kruger et al. 2012).

It has been suggested that the source J162634.17-242 328.7 (S1, #32) is a binary separated by 20–30 mas (see discussion in Ortiz-León et al. 2017). Our VLA *X* band image does not spatially resolve the individual binary components. We note that the secondary component was not detected in the most recent epochs covered by Ortiz-León et al. (2017).

For the sources we did not detect, we evaluated the 3σ upper limits, which varied across the mosaic field due to primary beam attenuation (see Table B.1). For 3σ rms levels as low as ∼15 μJy beam^{-1}, the detection statistics at 10 GHz in this region are 3/3 for Class 0 sources (100%), 5/8 for Class I YSOs (63%), 6/16 Class II sources (38%), and 2/5 Class III objects (40%).

Figure 3 shows the radio emission properties of the YSOs versus their *Spitzer* [3.6]–[4.5] colors (Evans et al. 2009). We see that the measured fluxes at 10 GHz of some sources are significantly brighter than the fluxes measured at 7.5 GHz by Dzib et al. (2013), while for other sources it is the opposite. The absence of a systematic trend indicates that our data are not likely to have been affected by flux calibration issues. We note that the classification of the continuous evolution of YSOs into Class 0/I, II, and III stages, taken from the literature, is to some extent artificial, and can be uncertain for YSOs that are transitioning from one stage to another. In addition, different catalogs or databases may report slightly different classifications, which are noted in Table B.1.

3.2. Nature of the emission at 10 GHz

In this section, we evaluate how much of the flux measured towards the YSOs in our 10 GHz VLA observations is due to: (i) thermal emission from dust, and (ii) other mechanisms such as free–free emission from ionized radio jets or photoevaporative winds, gyro-synchrotron emission from active magnetospheres, and synchrotron emission produced through the acceleration of cosmic-rays by jet or protostellar surface shocks (e.g., Macías et al. 2016; Gibb 1999; Forbrich et al. 2007; Padovani et al. 2016; Padovani & Galli 2018).

The brightest source in our sample, J162634.17-242 328.7 (S1, #32), has been already investigated in several studies and is known to be a completely non-thermal source. There is no evidence of a free–free component (e.g., André et al. 1988; Loinard et al. 2008; Ortiz-León et al. 2017). Indeed, the flux measured with the Very Long Baseline Array (VLBA) is systematically found to be equal to the VLA flux (Loinard et al. 2008; Ortiz-León et al. 2017). Since the VLBA is only sensitive to non-thermal emission, whereas the VLA is, in principle, sensitive to both thermal and non-thermal emission (e.g., Ortiz-León et al. 2017), the emission of this source is confirmed here as fully non-thermal. This source is, however, quite peculiar, since the non-thermal emission is not strongly variable, as has been confirmed in our observations (see Table B.1). This result is somewhat of a mystery, and may be due to a magnetic field that, in this specific case, is fossil-based rather than dynamo-driven (André et al. 1988). The former would explain S1's lack of flaring activity that would typically be seen in non-thermal
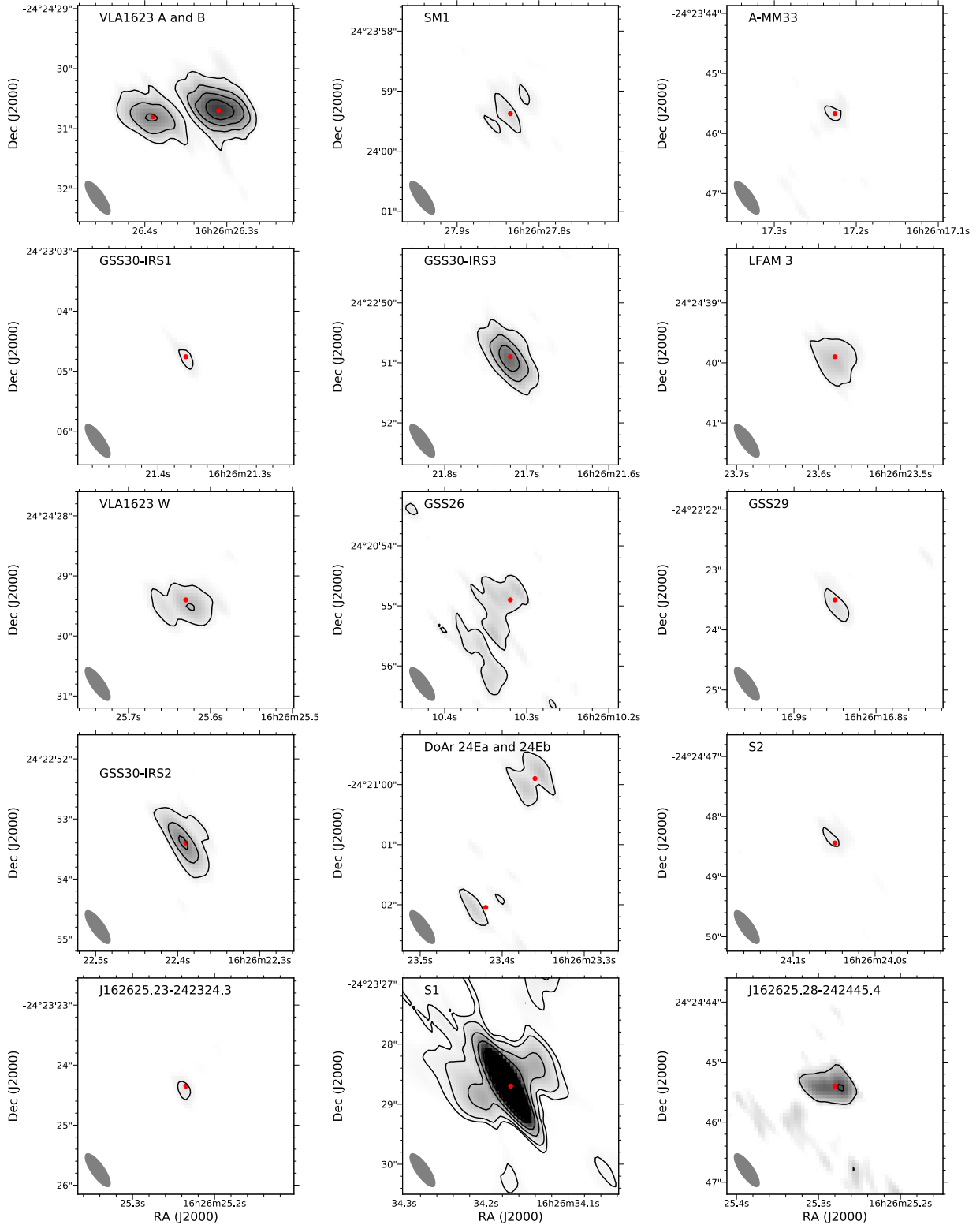
Fig. 2. Continuum observations of young stellar objects detected with VLA in band *X*. For all sources except S1, contours start from 5σ with a step of 5σ. For S1, contours are 10, 20, 50, 100, and 200σ. Greyscale images start at 3σ. The red dot corresponds to the coordinates used to name the sources in Table B.1. Last map (J162625.28-242 445.4) is for epoch 3 only.

sources otherwise. Given these extended studies focused on the S1 source, we do not discuss this here and further.

3.2.1. Contribution of thermal emission from dust

To determine the thermal contribution from dust, we assume that the ~107 GHz continuum fluxes reported by Kirk et al. (2017)

are entirely due to dust thermal emission, and then extrapolate the contribution of dust emission at our observing frequency of 10 GHz by assuming a power-law with a spectral index α (see Table B.1). We note that the angular resolution of the observations reported by Kirk et al. (2017) is approximately 10 times coarser than that of our VLA observations. Therefore,
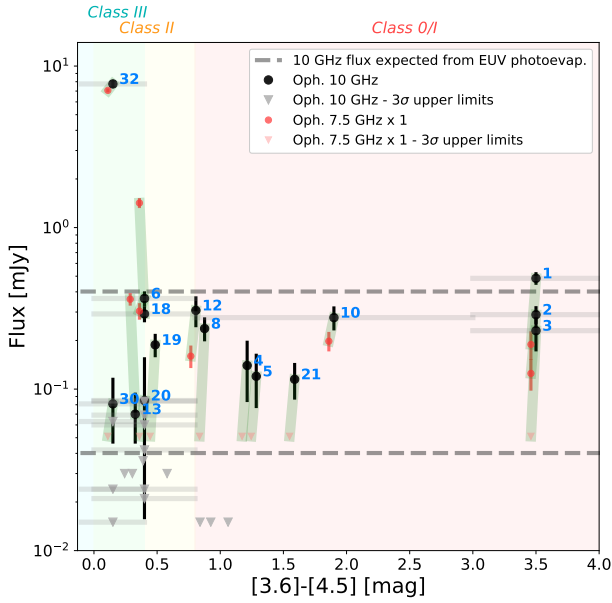
Fig. 3. Summary of observed 10 GHz radio fluxes. We show the characteristic [3.6]–[4.5] color ranges of the Class III, II, and 0/I YSOs as blue, yellow, and red filled regions which are bound in horizontal axis by [−0.4, 0.4], [0.0, 0.8], and [0.8, 4.0], respectively (overlapped area for Class III and II objects appears in green; see Allen et al. 2004). Our 10 GHz detections are presented as black circles. For sources we detected at 10 GHz, we also presented the fluxes measured at 7.5 GHz (red symbols) by Dzib et al. (2013). For the purposes of presentation, we offset the [3.6]–[4.5] values of the red symbols by −0.04. The observations towards the same target sources are linked by green lines. Gray and red downward triangles are the 3σ upper limits from these observations. Dashed lines show the expected radio fluxes from EUV photoevaporation winds from protoplanetary disks, assuming the EUV flux $\Phi_{EUV} = 10^{41}$ (*bottom*) and 10^{42} photons s^{-1} (*top*).

our estimates of 10 GHz dust emission should be regarded as the upper limits.

In the millimeter bands (e.g., ~90–350 GHz), the spectral indices of Class 0/I objects may be $\alpha = 2.5$–3 (see Chiang et al. 2012; Tobin et al. 2013, 2015; Miotello et al. 2014), while those of Class II/III objects may be lower ($\alpha = 2$–2.5; Ricci et al. 2010; Pérez et al. 2012; Tazzari et al. 2016) due to dust grain growth or high optical depths (see Li et al. 2017; Galván-Madrid et al. 2018). Taking this difference into account, we find that dust thermal emission could account for up to ~30% of the observed 10 GHz flux toward the Class 0 YSOs and is almost negligible in the Class III objects of our sample. For the Class I/II YSOs, the situation is more complex. In general, the contribution of the dust emission is ≤30% and in some cases, it is negligible. Exceptions, however, include the Class II sources J162610.32-242 054.9 (also known as GSS26, #12), for which dust emission could account for ~80% of the continuum flux at 10 GHz, and 162 618.98-242 414.3 (also called CRBR15, #16), for which the predicted dust emission is higher than the upper limit of $15\,\mu$Jy beam^{-1}, as well as two Class I sources (162625.49-242 301.6, #9 and 162 630.47-242 257.1, #11), for which the predicted dust emission fluxes are comparable to the measured upper limits of $15\,\mu$Jy beam^{-1} at 10 GHz. Therefore, except for a few Class I/II sources, the contribution from dust is in general ≤30% of the total emission. This behavior is consistent with even higher-angular resolution 870 μm ALMA observations toward the Class II sources J162623.36-242 059.9 (#19) and J162623.42-242 101.9 (#20, Cox et al. 2017), for which the dust

contribution at 10 GHz is also estimated to be ≤30% assuming dust spectral indices $\alpha = 2$–2.5.

3.2.2. Nature of the remaining radio emission

The remaining radio fluxes are likely to have contributions from (thermal) free–free emission from ionized radio jets, (thermal) free–free emission due to photoevaporative winds (e.g., Macías et al. 2016) or (non-thermal) gyro-synchrotron emission from stellar magnetospheres (e.g., Gibb 1999; Forbrich et al. 2007). Jet or protostellar surface shocks can also produce (non-thermal) synchrotron emission at our observing frequency, for example, through the acceleration of cosmic-rays (Carrasco-González et al. 2010; Padovani et al. 2016; Anglada et al. 2018). These radio emission mechanisms present specific characteristics, which we describe below.

Free–free emission from thermal jets and (gyro-)synchrotron emission are known to be time-variable (Forbrich et al. 2007; Dzib et al. 2013), but they may have very different characteristic timescales (Liu et al. 2014). Free–free emission may vary on time-scales from a few weeks to a few months considering the ionized gas recombination timescales as well as the dynamical timescales of the inner ~1 au disk. Gyro-synchrotron emission, however, is expected to vary on shorter timescales (minutes) due to flares on a stellar surface, and can vary up to the rotational periods of protostars. These periods can be as long as ~10 days, due to large magnetic loops coupling protostars and their inner disks (Forbrich et al. 2007; Liu et al. 2014). Synchrotron emission is also expected to be variable, although the timescale is unclear (Padovani et al. 2016).

Observations also indicate that the fluxes of thermal (free–free) sources rarely vary more than 20–30%, while, in general, non-thermal sources show greater variability (Ortiz-León et al. 2017; Tychoniec et al. 2018). The spectral indices of each type of emission can also differ. Free–free emission is characterized by spectral indices in the range [−0.1, 2.0], while gyro-synchrotron emission can span a significantly larger range of −5 to +2.5. Spectral indices $<−0.4$ have been observed in YSO jets and attributed to synchrotron emission (Anglada et al. 2018).

To probe the origins of the detected emission, we first checked if any of our sources had also been detected with the VLBA. As explained at the beginning of Sect. 3.2, any detection with the VLBA is necessarily non-thermal. In addition to S1, three other sources present in our observations: J162616.85-242 223.5 (GSS 29, #13), J162622.39-242 253.4 (GSS 30-IRS2, #18), and J162625.63-242 429.4 (VLA 1623 W, #10) are detected at 5 GHz with the VLBA (Ortiz-León et al. 2017) but they are undetected at 8 GHz (see Table 3). By comparing the VLBA fluxes to the VLA fluxes measured by Dzib et al. (2013), we find that the emission of J162616.85-242 223.5 (#13) could be fully non-thermal at 5 GHz. Unfortunately, no flux is available at 8 GHz for this source and we cannot rule out a fully non-thermal emission at 10 GHz. The emission of J162622.39-242 253.4 (#18) could be just partially non-thermal, as the VLBA flux is lower than the VLA flux (19% at 5 GHz and <6% at 8 GHz). Nevertheless, this ought to be considered carefully as this source may possibly be highly variable (Dzib et al. 2013) and because the observations were not carried out in a similar timeframe. The emission of J162625.63-242 429.4 (#10) could be fully non-thermal since at 5 GHz the VLBA emission is higher than the VLA flux, and the VLBA upper limit at 8 GHz is not lower than the VLA measurement even by a factor of 2.

Next, we determined the spectral indices of all sources between 10 GHz and 7.5 GHz and between 10 GHz and

Table 3. Comparison of fluxes (mJy) measured towards 3 YSOs with VLBA and VLA.

#	Source	VLBA[1] 5 GHz	VLA[2] 5 GHz	VLBA[1] 8 GHz	VLA[2] 8 GHz
10	J162625.63-242 429.4	0.66	0.22	<0.12	0.20
13	J162616.85-242 223.5	0.15–0.47[a]	0.34	…	0.36
18	J162622.39-242 253.4	0.30–0.38[a]	2.02	<0.09	1.42

Notes. [a]The flux of these sources is known to vary.
References. [1]From Ortiz-León et al. (2017). [2]From Dzib et al. (2013).

4.5 GHz, taking into account both the fit uncertainty and the calibration uncertainty (see Col. 3 in Table 4). The only two sources with negative spectral indices (J162616.85-242 223.5, #13 and J162622.39-242 253.4, #18) are those detected with the VLBA, which confirms the non-thermal origin of these sources' emission. Four sources, J162626.31-242 430.7 (#1), J162627.83-242 359.4 (#3), J162623.58-242 439.9 (#8), and J162623.36-242 059.9 (#19), show spectral indices higher than 2.5, which may indicate variability (see below).

Finally, we explored the long-term variability of the YSOs. Our observations were averaged over a couple of months and compared with those of Dzib et al. (2013) obtained in 2011. Dzib et al. (2013) reports that seven out of the 16 YSOs we detected are variable (see Table B.1, Col. 9). We note that among these variable sources, two have spectral indices between 7.5 and 10 GHz higher than 2.5. They also include the sources of non-thermal emission detected with the VLBA.

Any short-term variability will be explored in another paper by analyzing the 5 epochs separately, as well as more recent observations at lower spatial resolution. Nevertheless, to ensure that our conclusions are not affected by significant variability, we checked the maps of the different epochs individually. As expected, the faintest sources are barely detected or not detected at all depending on the noise level of each epoch. Among the brightest sources, even if some variations are observed for some, the fluxes vary around the values measured in the map with the combined epochs. We did not observe any cases where the flux is significantly higher at one epoch. The only exception is the source J162625.8-242 445.0 (#22), which is not detected in the map with the combined epochs, but clearly detected in epoch 3 with a flux of 0.4 mJy (see Fig. 2), which is probably due to a non-thermal flare.

To explore possible radio flux variations since the observations of Dzib et al. (2013), we extrapolate their fluxes at 7.5 GHz to those at 10 GHz, assuming that α is in the range of [−0.1, 2.0] (i.e., free–free emission from optically thin to optically thick limits) and compare the resulting values to our measured fluxes. For sources which were not detected at 7.5 GHz by Dzib et al. (2013), we evaluate the corresponding 3σ limits at 10 GHz assuming $\alpha = 2.0$, and compare the resulting values with our measurements (see Fig. 4). We find that there are three sources (J162626.31-242 430.7/#1, J162616.85-242 223.5/#13, and J162622.39-242 253.4/#18) detected in both our 10 GHz observations and the previous 7.5 GHz observations, for which the flux differences are too large to be explained by constant free–free emission. The emission of J162616.85-242 223.5 (#13), and J162622.39-242 253.4 (#18) is certainly non-thermal, as explained before. The emission of J162626.31-242 430.7 (#1) may be explained either by non-thermal radio emission or by thermal radio flux variability of more than

several tens of percent (see Fig. 4). In addition, after considering the spectral index range [−0.1, 2.0], it appears that three of our new radio detections (J162627.83-242 359.4/#3, J162623.58-242 439.9/#8, and J162623.36-242 059.9/#19) cannot be attributed to our improved sensitivity. The measured 10 GHz fluxes in the new VLA observations are significantly greater than 10 GHz fluxes scaled from the 7.5 GHz upper limit fluxes of Dzib et al. (2013) (see Fig. 4). Therefore, these detections were either due to variability or non-thermal, gyro-synchrotron spectral indices. The fractional radio flux variability of the sources can be seen in Fig. 4. We find that six out of our detected sources in the [3.6]–[4.5] color range of [0, 2] (i.e., late Class 0/I to early Class III stages) demonstrate over 50% fractional radio flux variability. The absolute values of their flux variations appear comparable to the observed flux variations from five epochs of observations towards CrA on the same date (Liu et al. 2014). The radio emission of some of these six sources (including J162625.63-242 429.4/#10, 162 616.85-242 223.5/#13, and J162622.39-242 253.4/#18) may be largely contributed by gyro-synchrotron emission, which can vary on short timescales.

Table 4 summarizes our conclusions regarding radio emission of the Oph A YSOs.

3.2.3. Association with X-ray emission

We checked the sources associated with X-ray emission (Imanishi et al. 2003, see Col. 10 in Table B.1). For Class III sources, X-ray emission mainly arises from magnetized stellar coronae, while in younger (Class I/II) sources, additional mechanisms can produce X-ray emission (e.g., shocks due to the material infalling from the disk to the stellar surface or due to the interaction of outflows with circumstellar material). All the Class II and III sources detected in our data are associated with X-ray emission, apart from J162623.42-242 102.0 (DoAr 24Eb, #20). The spatial resolution of the *Chandra* telescope might not be sufficient to separate its emission from J162623.36-242 059.9 (DoAr 24Ea). Among the younger sources we detected, only the Class I object J162623.58-242 439.9 (#8) was detected in X-ray.

4. Discussion: revisiting photoevaporation in Class II/III proto-planetary disks

High-energy stellar photons (UV or X-rays) may contribute to the dispersal of protoplanetary disks through photoevaporation (Hollenbach et al. 1994; Alexander et al. 2014). The exact contribution of this mechanism to disk dispersal and the way it impacts planet formation, however, need to be investigated further. Observations at radio wavelengths can probe the free–free emission from a disk surface that is partially or totally ionized by EUV photons or X-ray photons. Therefore, radio wavelength observations can serve as a powerful diagnostic of the contributions of these two types of photons in protoplanetary disk evolution. For example, Pascucci et al. (2012) predict the level of radio emission expected from photoevaporation driven by EUV photons or X-ray photons. Based on an analysis of 14 circumstellar disks, Pascucci et al. (2014) then determines that the EUV photoevaporation mechanism may not play a significant role in disk mass dispersal, when EUV photon luminosities (Φ_{EUV}) are lower than 10^{42} photons s^{-1}. Similar conclusions are obtained by Galván-Madrid et al. (2014) for ten disks toward the Corona Australis (CrA) star-forming region, inferring $\Phi_{EUV} < (1–4) \times 10^{41}$ photons s^{-1}, and by Macías et al. (2016) for the transitional disk of GM Aur ($\Phi_{EUV} \sim 6 \times 10^{40}$ photons s^{-1}).

Table 4. Summary of the emission of the YSOs.

#	Source	Spectral index α [1]	Dust	Ionized emission			X-ray detection [5]	ϕ_{EUV} [6]
				VLBA detection at 5 GHz [2]	Variability [3]	Fully or partially non-thermal emission [4]		(10^{40} erg s^{-1})
Class 0								
1	J162626.31-242 430.7	$3.3 \pm 0.7/1.2 \pm 0.3$	≤21%	N	Y	Y		
2	J162626.39-242 430.8	$2.9 \pm 0.8/1.5 \pm 0.5$	≤21%	N				
3	J162627.83-242 359.3	$\geq 4.8/\geq 1.7$	≤27%		Y	Y		
Class I								
4	J162617.24-242 346.0	$\geq 2.9/\geq 1.7$	≤28%					
5	J162621.36-242 304.7	$\geq 2.3/\geq 1.0$	≤8%					
6	J162621.72-242 250.9	$0.6 \pm 0.5/0.5 \pm 0.2$	≤23%	N	$Y_{4.5\,\mathrm{GHz}}$ [†]	Y		
7	162622.27-242 407.1	. . .	. . .					
8	J162623.58-242 439.9	$>4.2/0.8 \pm 0.3$	≤0.2%	N	Y	Y	Y	
9	162625.49-242 301.6	. . .	≤100%					
10	J162625.63-242 429.4	$1.2 \pm 0.7/0.3 \pm 0.2$	≤10%	Y	$Y_{7.5\,\mathrm{GHz}}$ [†]	Y		
11	162630.47-242 257.1	. . .	≤100%				Y	
Class II								
12	J162610.32-242 054.9	$2.3 \pm 0.6/1.4 \pm 0.2$	≤77%	N	Y [†]	Y	Y	<74
13	J162616.85-242 223.5	$-5.7 \pm 1.0/-1.9 \pm 0.4$	≤2%	Y	Y	Y	Y	
14	162617.06-242 021.6	. . .	. . .				Y	≲7
15	162618.82-242 610.5	. . .	. . .					≲7
16	162618.98-242 414.3	. . .	≤100%					≲4
17	162621.53-242 601.0	. . .	. . .				Y	≲7
18	J162622.39-242 253.4	$-5.5 \pm 0.4/-2.4 \pm 0.2$	≤0.5%	Y	Y	Y	Y	<71
19	J162623.36-242 059.9	$\geq 4.0/\geq 1.4$	≤18%		Y	Y	Y	<45
20	J162623.42-242 101.9	$\geq 0.8/\geq 0.3$	≤34%					≲21
21	J162624.04-242 448.5	$\geq 1.9/\geq 0.7$	≤1%				Y	≲28
22	J162625.28-242 445.4	. . .	. . .				Y	≲6
23	162627.81-242 641.8	. . .	. . .					≲9
24	162637.79-242 300.7	. . .	. . .					≲10
25	162642.74-242 427.7	. . .	. . .					≲14
26	162642.89-242 259.1	. . .	. . .					≲17
27	162643.86-242 450.7	. . .	. . .					≲21
Class III								
28	162615.81-241 922.1	. . .	. . .				Y	≲15
29	162622.19-242 352.4	. . .	. . .					≲4
30	J162625.23-242 324.3	$\geq 0.3/\geq 0.1$	≤2%				Y	≲20
31	162631.36-242 530.2	. . .	. . .				Y	≲6
32	J162634.17-242 328.7	$0.3 \pm 0.3/0.0 \pm 0.1$	≤0.02%	Y	N	Y	Y	

Notes. [1]The first spectral index is calculated between 7.5 and 10 GHz, the second between 4.5 and 10 GHz. The uncertainties take into account both the fit uncertainty and the calibration uncertainty. The spectral indices can be significantly affected by variability, as the measurements were carried out at several epochs. [2]Ortiz-León et al. (2017). Y for detection, N for non detection. [3]Dzib et al. (2013) and this study. The sources with the symbol. [†] Correspond to the sources that only present variability (>25%) in Dzib et al. (2013). [4]Y for the sources expected to present non-thermal emission based on the criteria discussed in the text (VLBA detection, variability, and spectral indices). Some of these sources could also be sources with thermal emission but abnormally high variability. [5]Imanishi et al. (2003). [6]EUV luminosities reaching the disks calculated from the fluxes or 3σ noise levels measured in our VLA images at 10 GHz (3 cm) and using Eq. (2) of Pascucci et al. (2012) and a distance of 137 pc for the Oph A cluster.

4.1. Constraints on EUV disk photoevaporation

The high sensitivity of our observations ($5\,\mu$Jy beam^{-1} at the center of the field of view) and the proximity of this cloud (137 pc) allow us to derive stringent constraints on the contribution of EUV photons on disk photoevaporation in the Oph A star-forming region. As explained before, the radio emission of five of our detected Class II/III sources (J162610.32-242 054.9/#12, J162616.85-242 223.5/#13, J162622.39-242 253.4/#18, J162623. 36-242 059.9/#19, and J162634.17-242 328.7/#32) is probably fully or partially non-thermal and we cannot exclude it for the three other detected sources. As such, the best constraints have come from the Class II/III objects we did not detect.
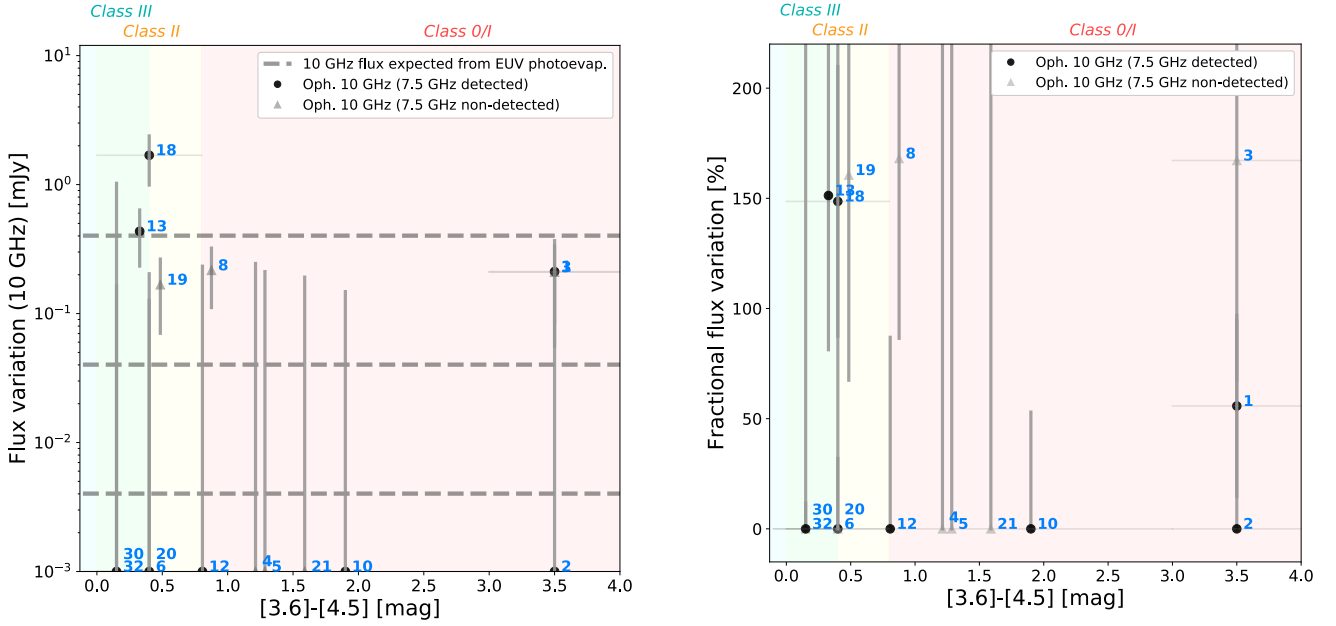
Fig. 4. Summary of observed radio flux variability (*left panel*) and fractional radio flux variability (*right panel*). We omitted sources which were not detected in both our 10 GHz observations and the previous 7.5 GHz observations of Dzib et al. (2013), since there is essentially no constraint on their time variability. For sources detected from at least one of those observations, we present the flux variation by calculating the average of the differences between the measured 10 GHz flux in our VLA observations and the expected 10 GHz flux derived by re-scaling the 7.5 GHz flux from Dzib et al. (2013) to 10 GHz assuming $\alpha = -0.1$ and 2.0. Vertical error bars take the measurement errors and the spectral index range $[-0.1, 2.0]$ into consideration. Dashed lines in the *left panel* show the expected radio fluxes from EUV photoevaporation winds from protoplanetary disks, assuming the EUV flux $\Phi_{\mathrm{EUV}} = 10^{40}$ (bottom), 10^{41} (middle), and 10^{42} photons s^{-1} (top).

Following the approach of Pascucci et al. (2014) and Galván-Madrid et al. (2014), we estimate the expected radio continuum fluxes $F_{10\,\mathrm{GHz}}$ for a particular EUV luminosity Φ_{EUV} based on the following formulation:

$$F_{10\,\mathrm{GHz}}\,[\mu\mathrm{Jy}] \sim 4.0 \times 10^{-40} \left(\frac{137}{d\,[\mathrm{pc}]}\right)^2 \left(\Phi_{\mathrm{EUV}}\,[\mathrm{s}^{-1}]\right) \left(\frac{10.0}{8.5}\right)^\alpha, \quad (1)$$

where d is the distance of the target source, and α is the spectral index of the free–free emission produced by the EUV photoevaporation. As an approximation, we tentatively consider $\alpha = 0$, and note that our estimate of $F_{10\,\mathrm{GHz}}$ is not especially sensitive to the exact value of α as long as α is in the range of $[-0.1, 2.0]$. We provide the estimates of $F_{10\,\mathrm{GHz}}$ at $\Phi_{\mathrm{EUV}} = 10^{40}$, 10^{41}, and 10^{42} photons s^{-1} for Figs. 3 and 4. For Class II and III sources which were not detected in our observations, the respective 3σ upper limits of $F_{10\,\mathrm{GHz}}$ constrained their Φ_{EUV} to be $\lesssim 4$–21×10^{40} photons s^{-1} (Fig. 3 and Table B.1). These upper limits are lower than those derived from previous observations toward CrA (<1–4×10^{41} photons s^{-1}, Galván-Madrid et al. 2014). We note that typical EUV photoevaporation models require Φ_{EUV} to be in the range of 10^{41}–10^{42} s^{-1} to disperse protoplanetary disks within a few Myrs (Font et al. 2004; Alexander et al. 2006; Alexander & Armitage 2009). EUV-driven photoevaporation is, consequently, very unlikely to play a major role in the dispersal of these disks.

For the Class II and III sources that are detected in our 10 GHz observations and do not necessarily exhibit nonthermal emission (J162623.42-242 102.0/#20, J162624.04-242 448.5/#21, and J162625.23-242 324.3/#30), if we assume that their 10 GHz fluxes are dominated by photoevaporation winds, the corresponding Φ_{EUV} values are well in the range required by the aforementioned models (Fig. 3). Hence, photoevaporation driven by EUV photons could be efficient enough

to disperse these disks. Presently, however, we do not have sufficient constraints on the spectral indices of these detected sources to be able to tell what fractions of their radio fluxes come from constant EUV photoevaporation winds. Observationally, we also do not know yet whether the radio emission associated with EUV photoevaporating disks evolves over time.

4.2. Constraints on X-ray disk photoevaporation

Photoevaporation by X-ray photons is another process that may lead to the dispersal of protoplanetary disks. We listed in Table B.1 the observed X-ray luminosities found in the literature for the YSOs of Oph A (Imanishi et al. 2003). They range over 0.01–3×10^{30} erg s^{-1}. Pascucci et al. (2012) determined the relation between the incident X-ray photon luminosity L_{X} and the resulting free–free emission that a disk would emit:

$$F_{10\,\mathrm{GHz}}\,[\mu\mathrm{Jy}] \sim 3.3 \times 10^{-30} \left(\frac{137}{d\,[\mathrm{pc}]}\right)^2 \left(L_{\mathrm{X}}\,[\mathrm{erg}\,\mathrm{s}^{-1}]\right) \left(\frac{10.0}{8.5}\right)^\alpha. \quad (2)$$

Based on this equation and the level of non-detections in our Class II objects, the upper limits derived for the incident X-ray photon luminosity are $\lesssim (7$–$25) \times 10^{30}$ erg s^{-1}, i.e. about 1–2 orders of magnitude higher than the observed values on average. Thus, we cannot exclude, with the present data, X-ray photoevaporation as a major mechanism in the dispersal of the disks. A series of more sensitive observations would be needed to determine its efficiency.

4.3. Studying the photoevaporation of protoplanetary disks with the Square Kilometre Array

In the future, the SKA will certainly revolutionize our understanding of the process of star and planet formation through radio

emission studies. Here we discuss the potential of the SKA to investigate the photoevaporation of disks.

The free–free emission produced by a disk (at the distance of Oph A) with an X-ray luminosity of more than 10^{29} erg s^{-1} could be detected, for example, with an rms of 0.1 μJy. Such a high level of sensitivity should be attainable in the future with the SKA. In particular, Hoare et al. (2015) estimates that a 1000-h deep field integration at the full resolution of SKA1-Mid ($\sim$40 mas, i.e. $\sim$5 AU for the disks of Oph A) over a 2×2.5 GHz bandwidth from 8.8 to 13.8 GHz would yield a noise level of 0.07 μJy beam^{-1}. Although the amount of time required appears significantly greater than the time dedicated to current radio projects, it should be noted that multiple projects will be carried out simultaneously with the SKA, and that a great number of sources will be covered in the same field with a single pointing. For example, the investigation of the photoevaporation in disk dispersal could be carried out simultaneously with high-priority studies of grain growth and the search for prebiotic molecules (Hoare et al. 2015).

With a single pointing, the SKA will cover a field of view of about 6 arcminutes (comparable to our four-pointing VLA mosaic). By targeting a rich region such as the Oph A cluster, a large number of disks (all the disks listed in this paper) can be observed simultaneously.

For bright radio emission sources, SKA will further provide good constraints on the instantaneous spectral indices over a wide range of frequency, useful data for gauging the fractional contributions of thermal and non-thermal emission mechanisms. An expansion of SKA1-Mid to $\sim$25 GHz would provide even stronger constraints on the spectral indices resolved across the young stars, spatially separating the different components. Complementary observations will also be possible with the next generation VLA (ng-VLA, Murphy et al. 2018; Selina et al. 2018) above the highest SKA1-Mid band.

In addition, shallow (e.g., rms $\sim$ few μJy) but regularly-scheduled SKA monitoring surveys will provide, for the first time, statistics on how much time Class 0–III YSOs remain in the radio active or inactive states, and on the levels of dominant radio emission mechanisms and radio flux variability levels during these states.

Finally, the SKA1-Mid resolution will be around 40 mas, hence, making it possible to spatially separate the different contributions from flares, jet, wind and disk to some degree. Simultaneous observations of hydrogen radio recombination lines at the high-angular resolution of the SKA will also enable the separation of ionized gas emission from dust emission in disks, which will be key for these kinds of studies.

Obtaining photoevaporation rates should, consequently, be achievable with the power of the SKA, however separating out the role of each type (EUV/X-ray) may be more complicated. According to Pascucci et al. (2012), the EUV contribution should be a factor ten higher than the X-ray contribution. Photoevaporation models predict different mass-loss profiles, but the subtraction of the EUV contribution to the free–free emission (necessary to investigate the X-ray driven photoevaporation of disks) could turn out to be highly uncertain, since the EUV luminosity is unknown.

5. Conclusions

We carried out very sensitive continuum observations of the Oph A star-forming region at 10 GHz with the VLA ($1\sigma = 5$ μJy beam^{-1} at the center of the field of view). We detected sixteen YSOs and two extragalactic candidate sources.

Seven of the detected YSOs had not been detected in a previous VLA survey of this region at 4.5 and 7.5 GHz by Dzib et al. (2013).

Using typical spectral indices for the possible components of radio emission, we constrained the origin of the emission detected at 10 GHz to the YSOs. In general, dust emission contributes less than 30% of the total emission. The 10 GHz emission appears to be mainly due to gyro-synchrotron emission from active magnetospheres, free–free emission from thermal jets or photoevaporative winds, or synchrotron emission due to accelerated cosmic-rays. Three of the YSOs show evidence of non-thermal emission. A comparison with the survey by Dzib et al. (2013) indicates that six of the sources show over 50% fractional radio flux variability, which is probably due to non-thermal emission.

The discussion surveys constraints on the EUV and X-ray photoevaporation mechanisms. For the Class II/III disks for which we detected no emission, the corresponding EUV luminosities are not sufficient to explain disk dispersal within a few Myrs through theoretical photoevaporation models. For the sources detected at 10 GHz (with a potentially significant contribution of ionized thermal emission), the corresponding maximum Φ_{EUV} values are within the range predicted by models. It is, however, currently unclear if EUV photoevaporating winds and their contributions to radio fluxes are constant over time. Even given the very high level of sensitivity in our observations, we have been unable to provide strong constraints on the efficiency of X-ray for disk dispersal. Observations of significantly greater sensitivity, which would also resolve the sources, are required to locate the different emission origins and constrain the efficiency of the photoevaporation mechanisms. With higher sensitivity and higher angular resolution, such future facilities as the SKA will make this a possibility.

References

Alexander, R. D., & Armitage, P. J. 2009, ApJ, 704, 989
Alexander, R. D., Clarke, C. J., & Pringle, J. E. 2006, MNRAS, 369, 229
Alexander, R., Pascucci, I., Andrews, S., Armitage, P., & Cieza, L. 2014, Protostars and Planets VI (Tucson: University of Arizona Press), 475

Allen, L. E., Calvet, N., D'Alessio, P., et al. 2004, ApJS, 154, 363
André, P., Montmerle, T., Feigelson, E. D., Stine, P. C., & Klein, K.-L. 1988, ApJ, 335, 940
Anglada, G., Rodríguez, L. F., & Carrasco-González, C. 2018, A&ARv, 26, 3
Ansdell, M., Williams, J. P., Trapman, L., et al. 2018, ApJ, 859, 21
Carrasco-González, C., Rodríguez, L. F., Anglada, G., et al. 2010, Science, 330, 1209
Chiang, H.-F., Looney, L. W., & Tobin, J. J. 2012, ApJ, 756, 168
Choi, M., Tatematsu, K., Hamaguchi, K., & Lee, J.-E. 2009, ApJ, 690, 1901
Cox, E. G., Harris, R. J., Looney, L. W., et al. 2017, ApJ, 851, 83
Dzib, S. A., Loinard, L., Mioduszewski, A. J., et al. 2013, ApJ, 775, 63
Ercolano, B., Weber, M. L., & Owen, J. E. 2018, MNRAS, 473, L64
Evans, II, N. J., Dunham, M. M., Jørgensen, J. K., et al. 2009, ApJS, 181, 321
Font, A. S., McCarthy, I. G., Johnstone, D., & Ballantyne, D. R. 2004, ApJ, 607, 890
Forbrich, J., Massi, M., Ros, E., Brunthaler, A., & Menten, K. M. 2007, A&A, 469, 985
Forbrich, J., Reid, M. J., Menten, K. M., et al. 2017, ApJ, 844, 109
Friesen, R. K., Di Francesco, J., Bourke, T. L., et al. 2014, ApJ, 797, 27
Friesen, R. K., Pon, A., Bourke, T. L., et al. 2018, ApJ, 869, 158
Gagné, M., Skinner, S. L., & Daniel, K. J. 2004, ApJ, 613, 393
Galván-Madrid, R., Liu, H. B., Manara, C. F., et al. 2014, A&A, 570, L9
Galván-Madrid, R., Liu, H. B., Izquierdo, A. F., et al. 2018, ApJ, 868, 39
Gibb, A. G. 1999, MNRAS, 304, 1
Güdel, M. 2002, ARA&A, 40, 217
Guilloteau, S., Dutrey, A., Piétu, V., & Boehler, Y. 2011, A&A, 529, A105
Gutermuth, R. A., Megeath, S. T., Myers, P. C., et al. 2009, ApJS, 184, 18
Haisch, Jr. K. E., Jayawardhana, R., & Alves, J. 2005, ApJ, 627, L57
Hoare, M., Perez, L., Bourke, T. L., et al. 2015, Advancing Astrophysics with the Square Kilometre Array (AASKA14), 115
Hollenbach, D., Johnstone, D., Lizano, S., & Shu, F. 1994, ApJ, 428, 654
Hsieh, T.-H., & Lai, S.-P. 2013, ApJS, 205, 5
Imanishi, K., Nakajima, H., Tsujimoto, M., Koyama, K., & Tsuboi, Y. 2003, PASJ, 55, 653
Johansen, A., Blum, J., Tanaka, H., et al. 2014, Protostars and Planets VI (Tucson: University of Arizona Press), 547
Jørgensen, J. K., Johnstone, D., Kirk, H., et al. 2008, ApJ, 683, 822
Kirk, H., Dunham, M. M., Di Francesco, J., et al. 2017, ApJ, 838, 114
Kirk, H., Hatchell, J., Johnstone, D., et al. 2018, ApJS, 238, 8
Kruger, A. J., Richter, M. J., Seifahrt, A., et al. 2012, ApJ, 760, 88
Leous, J. A., Feigelson, E. D., Andre, P., & Montmerle, T. 1991, ApJ, 379, 683
Li, J. I., Liu, H. B., Hasegawa, Y., & Hirano, N. 2017, ApJ, 840, 72
Liu, H. B., Galván-Madrid, R., Forbrich, J., et al. 2014, ApJ, 780, 155
Loinard, L., Torres, R. M., Mioduszewski, A. J., & Rodríguez, L. F. 2008, ApJ, 675, L29
Macías, E., Anglada, G., Osorio, M., et al. 2016, ApJ, 829, 1
McMullin, J. P., Waters, B., Schiebel, D., Young, W., & Golap, K. 2007, in Astronomical Data Analysis Software and Systems XVI, eds. R. A. Shaw, F. Hill, & D. J. Bell, ASP Conf. Ser., 376, 127
Miotello, A., Testi, L., Lodato, G., et al. 2014, A&A, 567, A32
Motte, F., Andre, P., & Neri, R. 1998, A&A, 336, 150
Murphy, E. J., Bolatto, A., Chatterjee, S., et al. 2018, in Science with a Next Generation Very Large Array, ed. E. Murphy, ASP Conf. Ser., 517, 3
Ortiz-León, G. N., Loinard, L., Kounkel, M. A., et al. 2017, ApJ, 834, 141
Owen, J. E., Ercolano, B., & Clarke, C. J. 2011, MNRAS, 412, 13
Owen, J. E., Clarke, C. J., & Ercolano, B. 2012, MNRAS, 422, 1880
Padovani, M., & Galli, D. 2018, A&A, 620, L4
Padovani, M., Marcowith, A., Hennebelle, P., & Ferrière, K. 2016, A&A, 590, A8
Pascucci, I., Gorti, U., & Hollenbach, D. 2012, ApJ, 751, L42
Pascucci, I., Ricci, L., Gorti, U., et al. 2014, ApJ, 795, 1
Pascucci, I., Testi, L., Herczeg, G. J., et al. 2016, ApJ, 831, 125
Pattle, K., Ward-Thompson, D., Kirk, J. M., et al. 2015, MNRAS, 450, 1094
Pérez, L. M., Carpenter, J. M., Chandler, C. J., et al. 2012, ApJ, 760, L17
Ribas, Á., Bouy, H., & Merín, B. 2015, A&A, 576, A52
Ricci, L., Testi, L., Natta, A., & Brooks, K. J. 2010, A&A, 521, A66
Russell, S. S., Hartmann, L., Cuzzi, J., et al. 2006, Timescales of the Solar Protoplanetary Disk, eds. D. S. Lauretta, & H. Y. McSween (Tucson: University of Arizona Press), 233
Selina, R. J., Murphy, E. J., McKinnon, M., et al. 2018, in Science with a Next Generation Very Large Array, ed. E. Murphy, ASP Conf. Ser., 517, 15
Strom, K. M., Strom, S. E., Edwards, S., Cabrit, S., & Skrutskie, M. F. 1989, AJ, 97, 1451
Tazzari, M., Testi, L., Ercolano, B., et al. 2016, A&A, 588, A53
Testi, L., Birnstiel, T., Ricci, L., et al. 2014, Protostars and Planets VI (Tucson: University of Arizona Press), 339
Tobin, J. J., Dunham, M. M., Looney, L. W., et al. 2015, ApJ, 798, 61
Tobin, J. J., Chandler, C. J., Wilner, D. J., et al. 2013, ApJ, 779, 93
Tychoniec, Ł., Tobin, J. J., Karska, A., et al. 2018, ApJS, 238, 19
van der Marel, N., Williams, J. P., Ansdell, M., et al. 2018, ApJ, 854, 177
Wilking, B. A., Gagné, M., & Allen, L. E. 2008, Star Formation in the ρ Ophiuchi Molecular Cloud (California: Astronomical Society of the Pacific), 351
Williams, J. P., & Cieza, L. A. 2011, ARA&A, 49, 67

[1] Laboratoire d'Astrophysique de Bordeaux, Univ. Bordeaux, CNRS, B18N, allée Geoffroy Saint-Hilaire, 33615 Pessac, France
e-mail: audrey.coutens@u-bordeaux.fr
[2] European Southern Observatory (ESO), Karl-Schwarzschild-Str. 2, 85748 Garching, Germany
[3] School of Physics and Astronomy, Queen Mary University of London, Mile End Road, London E1 4NS, UK
[4] SKA Organisation, Jodrell Bank Observatory, Lower Withington, Macclesfield, Cheshire SK11 9DL, UK
[5] Centre for Astrophysics Research, University of Hertfordshire, College Lane, Hatfield AL10 9AB, UK
[6] School of Physics and Astronomy, University of Leeds, Leeds LS2 9JT, UK
[7] Instituto de Radioastronomía y Astrofísica, Universidad Nacional Autónoma de México, Morelia 58089, México
[8] Instituto de Astronomía, Universidad Nacional Autónoma de Mexico, Apartado Postal 70-264, Ciudad de México 04510, México
[9] INAF – Osservatorio Astrofisico di Arcetri, Largo Enrico Fermi 5, 50125 Florence, Italy
[10] Department of Astronomy, University of Geneva, Ch. des Maillettes 51, 1290 Versoix, Switzerland
[11] Department of Astronomy, University of Geneva, Ch. d'Ecogia 16, 1290 Versoix, Switzerland
[12] Max-Planck-Institüt für extraterrestrische Physik, Giessenbachstrasse 1, 85748 Garching, Germany
[13] Observatorio Astronómico Nacional (OAG-IGN), Alfonso XII 3, 28014 Madrid, Spain
[14] Université Grenoble Alpes, Institut de Planétologie et d'Astrophysique de Grenoble (IPAG), 38401 Grenoble, France
[15] NRC Herzberg Astronomy and Astrophysics, 5071 West Saanich Rd, Victoria, BC, V9E 2E7, Canada
[16] Department of Physics and Astronomy, University of Victoria, Victoria, BC, V8P 5C2, Canada
[17] Leiden Observatory, Leiden University, PO Box 9513, 2300 RA Leiden, The Netherlands
[18] Anton Pannekoek Institute for Astronomy, University of Amsterdam, Science Park 904, 1098 XH Amsterdam, The Netherlands
[19] Lund Observatory, Lund University, Box 43, 22100 Lund, Sweden
[20] Centre for Astrophysics and Supercomputing, Swinburne University of Technology, Hawthorn, Victoria 3122, Australia
[21] Departamento de Astronomía, Universidad de Chile, Camino El Observatorio 1515, Las Condes, Santiago, Chile
[22] Ural Federal University, 620002, 19 Mira street, Yekaterinburg, Russia
[23] Department of Physics and Astronomy, University College London, Gower St., London WC1E 6BT, UK
[24] Department of Chemistry, Ludwig Maximilian University, Butenandtstr. 5–13, 81377 München, Germany
[25] Max Planck Institute for Astronomy, Königstuhl 17, 69117, Heidelberg, Germany
[26] Institute of Astronomy, University of Cambridge, Madingley Road, CB3 0HA, Cambridge, UK
[27] NRAO, 520 Edgemont Road Charlottesville, VA 22903-2475 USA
[28] ASTRON Netherlands Institute for Radio Astronomy, Oude Hoogeveensedijk 4, 7991 PD Dwingeloo, The Netherlands
[29] Joint Institute for VLBI ERIC (JIVE), Oude Hoogeveensedijk 4, 7991 PD Dwingeloo, The Netherlands
[30] Department of Space, Earth and Environment, Chalmers University of Technology, Onsala Space Observatory, 439 92 Onsala, Sweden
[31] Harvard-Smithsonian Center for Astrophysics, 60 Garden Street, Cambridge, MA 02 138, USA

Appendix A: Image component sizes obtained with imfit

Table A.1. Image component sizes (deconvolved from beam) obtained with imfit.

#	Source	Major axis *FWHM* ($''$)	Minor axis *FWHM* ($''$)	Position angle ($°$)
1	J162626.31-242 430.7	0.78 ± 0.09	0.52 ± 0.09	76 ± 15
2	J162626.39-242 430.8	0.83 ± 0.14	0.45 ± 0.11	67 ± 16
6	J162621.72-242 250.9	0.97 ± 0.11	0.57 ± 0.05	37 ± 8
8	J162623.58-242 439.9	0.94 ± 0.20	0.75 ± 0.14	36 ± 77
10	J162625.63-242 429.4	1.06 ± 0.22	0.69 ± 0.23	85 ± 28
18	J162622.39-242 253.4	1.08 ± 0.14	0.52 ± 0.05	26 ± 6
21	J162624.04-242 448.5	1.37 ± 0.40	0.47 ± 0.15	52 ± 12
32	J162634.17-242 328.7	0.65 ± 0.02	0.09 ± 0.01	25.6 ± 0.5
42	J162635.33-242 405.3	0.55 ± 0.14	0.25 ± 0.07	50 ± 16

Notes. Sources are listed in the same order as in Table B.1.

Appendix B: Additional table

Table B.1. Catalog of sources observed in field of view of our observations grouped in categories.

#	Source [0] (J2000 coordinates)	Flux (mJy) [1] 10.0 GHz	Flux (mJy) [1] 7.5 GHz	Flux (mJy) [1] 4.5 GHz	Flux (mJy) [1] 107 GHz	Source type [2]	Refs. [3]	Variable [4]	L_X [5] (10^{29} erg s^{-1})	Other names
1	J162626.31-242 430.7	0.485 ± 0.033	0.189 ± 0.034	0.189 ± 0.034	59.82 ± 0.47 [1]	YSO 0? [8]	a	Y		VLA1623 B
2	J162626.39-242 430.8	0.289 ± 0.030	0.125 ± 0.025	0.087 ± 0.030	59.82 ± 0.47 [1]	YSO 0	a	U		VLA1623 A
3	J162627.83-242 359.4	0.230 [7]	≤ 0.051	≤ 0.051	23.13 ± 0.46	YSO/PC [9]	b			SM1
4	J162617.23-242 345.7	0.140 [7]	≤ 0.051	≤ 0.051	14.46 ± 0.29	YSO I	c,d			A-MM33, CRBR12, ISO-Oph 21
5	J162621.36-242 304.7	0.120 [7]	≤ 0.051	≤ 0.051	3.48 ± 0.67	YSO I/0-I	c/d			GSS 30-IRS1, Elias 21
6	J162621.72-242 250.9	0.364 ± 0.030	0.304 ± 0.029	0.238 ± 0.017	30.71 ± 0.63	YSO I/FS	a/c	Y$_{4.5GHz}$ [10]		GSS 30-IRS3, LFAM1
7	162622.27-242 407.1	≤ 0.015	≤ 0.051	≤ 0.051	≤ 0.16	YSO I-FS	c			CRBR25
8	J162623.58-242 439.9	0.237 ± 0.035	< 0.06	0.125 ± 0.015	≤ 0.16	YSO 0-I/FS	d/a,c	Y	10.8	LFAM 3
9	162625.49-242 301.6	≤ 0.051	≤ 0.051	≤ 0.051	9.17 ± 0.44	YSO I	c			CRBR36
10	J162625.63-242 429.4	0.277 ± 0.041	0.198 ± 0.023	0.218 ± 0.014	11.24 ± 0.44	YSO I	a,d	Y$_{7.5GHz}$ [10]		VLA1623 W, LFAM 4
11	162630.47-242 257.1	≤ 0.021	≤ 0.051	≤ 0.051	11.22 ± 0.44	YSO FS/0-I	c/d		4.8	...
12	J162610.32-242 054.9	0.307 [7]	0.160 ± 0.022	0.100 ± 0.012	27.25 ± 0.35	YSO II	a,c,d	Y	9.5	GSS 26
13	J162616.85-242 223.5	0.070 [7]	0.360 ± 0.024	0.337 ± 0.017	≤ 0.16	YSO II	a,c,d	Y	16.3	GSS 29, LFAM p1
14	162617.06-242 021.6	≤ 0.030	≤ 0.051	≤ 0.051	≤ 0.16	YSO II	c		10.7	DoAr 24
15	162618.82-242 610.5	≤ 0.030	≤ 0.051	≤ 0.051	≤ 0.16	YSO II	c			...
16	162618.98-242 414.3	≤ 0.015	≤ 0.051	≤ 0.051	5.96 ± 0.98	YSO II-FS	c			CRBR15
17	162621.53-242 601.0	≤ 0.030	≤ 0.051	≤ 0.051	...	YSO II	c		0.1–0.6	...
18	J162622.39-242 253.4	0.292 ± 0.027	1.42 ± 0.07	2.02 ± 0.10	≤ 0.16	YSO II	a,c	Y	51.5	GSS 30-IRS2, VSSG12, ISO-Oph 34, LFAM 2
19	J162623.36-242 059.9 [6]	0.188 [7]	≤ 0.051	≤ 0.051	...	YSO II	c,d		4.7	GSS 31a, DoAr 24Ea
20	J162623.42-242 102.0	0.085 [7]	≤ 0.051	≤ 0.051	...	YSO II?	e			GSS 31b, DoAr 24Eb
21	J162624.04-242 448.5	0.115 ± 0.027	≤ 0.051	≤ 0.051	≤ 0.16	YSO II/FS	c/d		29.2	S2
22	J162625.28-242 445.4 [11]	≤ 0.024	≤ 0.051	≤ 0.051	≤ 0.16	YSO II	c		0.5	...
23	162627.81-242 641.8	≤ 0.036	≤ 0.051	≤ 0.051	...	YSO II	c			...
24	162637.79-242 300.7	≤ 0.042	≤ 0.051	≤ 0.051	≤ 0.16	YSO II	c			LFAM p2
25	162642.74-242 427.7	≤ 0.060	≤ 0.051	≤ 0.051	≤ 0.16	YSO II	c			...
26	162642.89-242 259.1	≤ 0.069	≤ 0.051	≤ 0.051	≤ 0.16	YSO II	c			...
27	162643.86-242 450.7	≤ 0.084	≤ 0.051	≤ 0.051	≤ 0.16	YSO II	c			...
28	162615.81-241 922.1	≤ 0.063	≤ 0.051	≤ 0.051	≤ 0.16	YSO III	c		3.1	...
29	162622.19-242 352.4	≤ 0.015	≤ 0.051	≤ 0.051	≤ 0.16	YSO III	c			...
30	J162625.23-242 324.3	0.081 [7]	≤ 0.051	≤ 0.051	≤ 0.16	YSO III/FS	c/d		6.0	...
31	162631.36-242 530.2	≤ 0.024	≤ 0.051	≤ 0.051	≤ 0.16	YSO III	c		0.2	...
32	J162634.17-242 328.7	7.75 ± 0.11	7.07 ± 0.35	7.98 ± 0.40	≤ 0.16	YSO III	a,c	N	22.6	S1
33	162614.63-242 507.5	≤ 0.024	≤ 0.051	≤ 0.051	≤ 0.16	YSO U	f			...
34	162625.99-242 340.5	≤ 0.015	≤ 0.051	≤ 0.051	≤ 0.16	YSO U	g			...
35	162632.53-242 635.4	≤ 0.045	≤ 0.051	≤ 0.051	≤ 0.16	YSO U	c			CRBR40
36	162638.80-242 322.7	≤ 0.045	≤ 0.051	≤ 0.051	...	YSO U	c			...
37	162639.92-242 233.4	≤ 0.078	≤ 0.051	≤ 0.051	...	YSO U	c			...
38	162608.04-242 523.1	≤ 0.051	≤ 0.05	0.103 ± 0.014		EG?	a	Y		
39	J162629.62-242 317.3	0.091 [4]	0.124 ± 0.018	0.228 ± 0.014		EG?	a	Y		
40	J162630.59-242 023.0	≤ 0.045	0.064 ± 0.017	0.098 ± 0.013		EG?	a	Y		
41	J162634.95-242 655.3	≤ 0.069	0.100 ± 0.013	0.197 ± 0.019		EG?	a	Y		
42	J162635.33-242 405.3	0.377 ± 0.039	0.329 ± 0.033	0.650 ± 0.038		EG?	a	Y		

Notes. [0]The source name starts with J when detected with the VLA, either in this study or in Dzib et al. (2013). The rest of the name correspond to the J2000 RA-Dec coordinates hhmmss.ss-ddmmss.s. When undetected with VLA, we used the coordinates given in the references listed in Col. 8. [1]The fluxes measured at 10.0 GHz were derived with Gaussian fit. The uncertainties correspond to the fit uncertainties only. The fluxes measured at 4.5 and 7.5 GHz come from Dzib et al. (2013), while the ones at 107 GHz come from Kirk et al. (2017). It should be noted that the flux measured at 107 GHz for J162626.31-242 430.7 and J162626.39-242 430.8 includes the two sources. The upper limits correspond to the 3σ levels ($1\sigma = 17$ μJy beam^{-1} for both frequencies) measured in the three-epoch combined images from Dzib et al. (2013). [2]The source is either YSO (Young Stellar Object) or EG (Extragalactic candidate). The YSOs are classified into: PC (prestellar core), 0 (Class 0 protostar), I (Class I protostar), FS (Flat Spectrum), II (Class II protostar), III (Class III protostar), U (Unknown classification for the YSO candidates). [4]Variability taken from Dzib et al. (2013). A source is considered variable when its variability fraction is $\geq$25%. Legend: Y – variable; N – not variable; U – unknown. [5]X-ray luminosity in the 0.5–9.0 keV (Imanishi et al. 2003). [6]This source could be a binary. The flux given here corresponds to the total flux. [7]Contrary to the other sources, the fluxes of these objects were integrated over a circular area selected with CASA due to their particular structure, which may be caused by residual phase errors, or due to a very uncertain Gaussian fit. [8]This source may be a young star or an outflow knot feature. [9]This source was proposed to contain an extremely young, deeply embedded protostellar object (Friesen et al. 2014). [10]Source variable only at the indicated frequency. [11]Source only detected in epoch 3 with a flux of 0.4 Jy.

References. [3]References for the YSO classification : (a) Dzib et al. (2013), (b) Friesen et al. (2014), (c) Wilking et al. (2008), (d) Hsieh & Lai (2013), (e) Kruger et al. (2012), (f) Jørgensen et al. (2008), (g) Evans et al. (2009).